



Enhanced refractometer for aqueous solutions based on perfluorinated polymer optical fibres

PABLO ROLDÁN-VARONA,^{1,2,3,*}  MAURO LOMER,^{1,2,3} JOSÉ FRANCISCO ALGORRI,^{1,2,3}  LUIS RODRÍGUEZ-COBO,² AND JOSÉ MIGUEL LÓPEZ-HIGUERA^{1,2,3} 

¹Photonics Engineering Group, University of Cantabria, 39005 Santander, Spain

²CIBER-bbn, Instituto de Salud Carlos III, 28029 Madrid, Spain

³Instituto de Investigación Sanitaria Valdecilla (IDIVAL), 39011 Santander, Spain

*pablo.rolدان@unican.es

Abstract: The use of the new CYTOP (Cyclized Transparent Optical Polymer) fibres for the inscription of optical structures and the detection of different parameters has started to gain importance in the past decade. This work presents the design, simulation and manufacture of a CYTOP-based surrounding refractive index sensor for aqueous solutions, given its high sensitivity in the range 1.315 – 1.333 (at 1550 nm wavelength). The structure is based on a bent and polished fibre (in order to increase its sensitivity), the polished area being the surface on which a diffraction grating is inscribed with a femtosecond laser. The interaction of the field propagated by the fibre with the grating causes diffraction of certain orders towards the outside, depending, among other things, on the refractive index of the fluid. In addition to a maximum sensitivity of -208.8 nm/RIU and a remarkable insensitivity to temperature, it offers a spectral fingerprint of each sensed fluid.

© 2022 Optica Publishing Group under the terms of the [Optica Open Access Publishing Agreement](#)

1. Introduction

A great attention and research effort have been drawn to the transducing properties of optical fibres, which has made possible a breakthrough in the last 50 years with respect to optical fibre sensors (OFSs), whether in glass fibre [1] or plastic optical fibre (POF) [2,3]. Its electrical immunity, small transmission loss, remote sensing, and high sensitivity, outperform other more traditional schemes. Moreover, the discovery of new materials in fibres, which improve their optical properties, allow their application in increasingly varied fields, whether in the scope of engineering, industry, medicine, or biochemistry, among others.

Regarding plastic optical fibres, poly(methyl methacrylate) (PMMA) has traditionally been used. The first fibres based on PMMA cores emerged in the 1960s, and their growth has been extraordinary to this day. In contrast to glass fibres, POF stands out for its ease of handling, flexibility, and reduced price [2,4]. Likewise, the improvement of the manufacturing process has considerably limited their attenuation, and they can be used for short-haul communications or optical fibre sensors.

However, in the late 1990s Asahi Glass Co (currently ACG Inc.) developed a special type of POF, based on an amorphous fluorinated polymer called CYTOP [5,6]. It is poly(perfluorobutenylvinyl ether). Characterized by a refractive index of ~ 1.34 , it stands out for its compatibility with the aqueous index regime, an important feature for biosensing [7]. Moreover, it has a very low near-infrared attenuation (~ 10 dB/km) and a transmission bandwidth of up to 1300 nm. It is a graded-index polymer optical fibre (GI-POF), with less modal noise and material dispersion than PMMA fibers [2]. The use of CYTOP fibres began to gain important relevance in the 2010s (Table 1), so it is a field with a great future projection. In recent years, the inscription of optical structures using femtosecond lasers in CYTOP fibres for the development of OFSS stands out [8].

Table 1 lists the most important works in the literature. As it can be seen, the works are recent, and most of them use fibre Bragg gratings (FBGs) as the sensing structure.

Table 1. Works related to the manufacture of optical structures in CYTOP fibres by means of femtosecond laser.

Ref.	Year	Optical structure	Parameter sensed	Sensitivity
[9]	2021	FBG ^a	Temperature	27.5 $\frac{\text{pm}}{\text{°C}}$ (10 – 60 °C)
[10]	2020	FBG	γ radiation	–26.2 pm/kGy (0 – 41 kGy)
[11]	2020	FBG and FPI ^b	Bending angle	–3.9 pm/° (0 – 90 °)
[12]	2020	CFBG ^c	Force and liquid level	200 N range 50 cm range
[13]	2019	FBG array	Torque and displacement	8.8 · 10 ^{–2} $\frac{\text{nm}}{\text{Nm}}$
[14]	2018	FPI	Strain and temperature	1.35 $\frac{\text{pm}}{\mu\epsilon}$ (0 – 5040 $\mu\epsilon$) 26.4 $\frac{\text{pm}}{\text{°C}}$ (40 – 60 °C)
[15]	2017	FBG	Vibration	–
[7]	2015	FBG	Strain	1.3 pm/ $\mu\epsilon$ (0 – 50 $\mu\epsilon$)

^aFiber Bragg grating;

^bFabry-Perot interferometer;

^cChirped FBG.

In this work, an optical structure based on a perfluorinated POF is designed, simulated and manufactured using a femtosecond laser. Taking advantage of its infrared transmission, the device is used as a highly-sensitive refractive index sensor in aqueous solutions, thus having potential applicability in the field of biomedicine [16]. To this end, in addition to increasing sensitivity to the external medium by bending the fibre and polishing its cladding, a diffraction grating is inscribed into the previously polished area. The variability of the transmitted diffraction orders provides a spectral fingerprint of the different aqueous solutions, which can be used for the sensing of their refractive index, among others.

2. Optical structure design

The designed optical structure is the one depicted in Fig. 1. The dimensions of the CYTOP fibre used are listed below. The graded-index core has a diameter $d_{core} = 120 \mu\text{m}$, while the cladding has a thickness of $20 \mu\text{m}$ ($d_{clad} = 160 \mu\text{m}$). Likewise, there is a polycarbonate protection overcladding with a total diameter $d_{oc} = 490 \mu\text{m}$. The fibre, measured in transmission, was placed with a curvature defined by a radius of curvature (ROC) R . To fix the fibre, two PMMA bulks were manufactured with the groove where the fibre was placed, closing the sandwich-structure with epoxy resin.

Subsequently, the PMMA bulk corresponding to $\Psi = 90^\circ$ started to be polished (first with ultra-fine grit sandpaper, P4000; and then with $12 \mu\text{m}$ lapping film). ϵ refers to the depth of polish. At the moment in which the outer interface of the fibre is reached, $\epsilon = 0$. When polishing continued ($\epsilon > 0$), the polished part of the fibre began to generate an elliptical shape in the XY plane. To determine the polishing depth (ϵ), the dimensions of the ellipse generated were considered, specifically their minor and major axes. The geometric and trigonometric

Table 2. Simulation parameters used in RSoft for both cases (R-sweep and ϵ -sweep).^a

• COMMON PARAMETERS			
d_{core}	120 μm	$n_{core}(r)$	$1.352\sqrt{1 - 2\Delta\frac{4r^2}{d_{core}^2}}$
d_{clad}	160 μm	n_{clad}	1.34
d_{oc}	∞	n_{oc}	1.58
Ψ	$[0, 180]^\circ$	λ	1550 nm
• R-SWEEP SIMULATION (3-D)			
ϵ	0 μm	R	{1 : 10, 20} mm
• ϵ -SWEEP SIMULATION (2-D)			
R	5 mm	ϵ	{0 : 10 : 60} μm
SRI	[1, 1.36]		

^a r : radial distance to the axial axis of the fibre; $\Delta = \frac{(n_{core})_{max}^2 - n_{clad}^2}{2(n_{core})_{max}^2}$.

It should be noted that in both cases, in order to make the bending simulation feasible in BPM, a mathematical coordinate transformation called conformal mapping is used [18,19]. The transformation used, that preserves the angle between oriented curves, is as follows:

$$W = u + iv = f(Z) = f(x + iy) = R \cdot \ln\left(\frac{Z}{R}\right), \tag{3}$$

for which

$$\left|\frac{dZ}{dW}\right| = \exp\left(\frac{u}{R}\right). \tag{4}$$

In this way, the fibre curvature can be modelled from a tilted refractive index profile, achieving a translation invariance in light propagation direction. The tilted RI profile (n_{tilt}) as a consequence of the transformation is obtained by multiplying the actual RI of the material (n_{real}) by Eq. (4):

$$n_{tilt}(u, v) = n_{real}(u, v) \cdot \exp\left(\frac{u}{R}\right) \approx n_{real}(u, v) \left(1 + \frac{u}{R}\right). \tag{5}$$

\uparrow
 $d_{clad} \ll R$

Figure 3 depicts, for both unpolished (R-sweep, Fig. 3(a)) and polished (ϵ -sweep, Fig. 3(b)) fibre, a schematic of the fibre in the Z-plane (no transformation) and in the W-plane (conformal mapping applied), as well as the corresponding refractive index profiles. The RI profile in Fig. 3(b) corresponds to a polished fibre in the $\Psi = 90^\circ$ position. Fibre polishing centered at $\Psi = 90^\circ$ is mathematically associated with the function shown below (defined in the Z-plane), in polar coordinates. The limits of θ are defined from trigonometric relations obtained according to Fig. 2(a).

$$r(\theta) = \frac{R + \frac{d_{clad}}{2} - \epsilon}{\sin \theta}, \quad \theta \in \left[\frac{\pi}{2} - \alpha, \frac{\pi}{2} + \alpha\right], \tag{6}$$

with $\alpha = \cos^{-1}\left(\frac{R + \frac{d_{clad}}{2} - \epsilon}{R + \frac{d_{clad}}{2}}\right)$. Accordingly, $\delta = 2R\alpha$.

Once conformal mapping has been defined, the simulations are carried out. First of all, regarding the ROC, a value of R must be chosen such that it causes relevant bending losses. In this case, an increase in attenuation is the basis of many optical sensors, due to the high

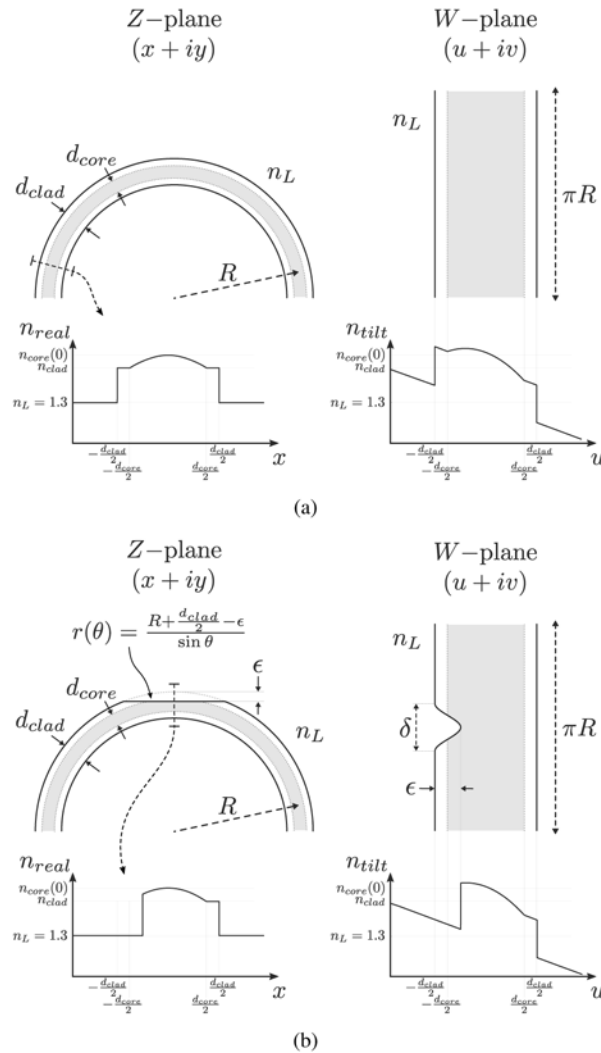


Fig. 3. Schematic of the fibre in the Z-plane (no transformation) and in the W-plane (conformal mapping applied) for (a) unpolished (R -sweep simulation), (b) and polished (at $\Psi = 90^\circ$) fibre (ϵ -sweep simulation). Refractive index profiles are depicted for each case (with and without transformation).

sensitivity achieved to detect variations in the surrounding medium. Figure 4 depicts the simulated cross-section of the fibre (core and cladding) at $\Psi = 90^\circ$ (polishing position) for different values of R .

It can be seen that extremely small R values (e.g. 2 mm) result in excessive sensing attenuation (>15 dB), as well as greater ease of fibre breakage. On the other hand, bending radii larger than 6 mm make the power propagate more easily along the axial axis of the fibre (GI-POF), with less dependence of the bending losses on the outer refractive index. Consequently, the optimum bending radii are around 5 mm, which is the value chosen. For this value, a noticeable presence of propagated cladding modes can be observed, which, after polishing, will be dependent on the surrounding refractive index (SRI).

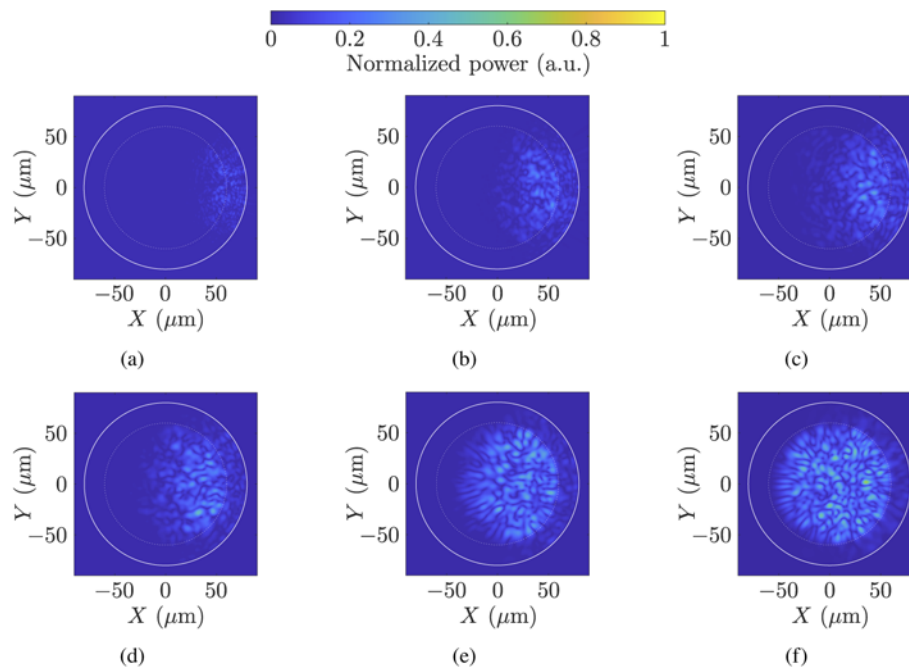


Fig. 4. RSoft simulation of the resulting field in the fibre cross-section at $\Psi = 90^\circ$ for bending radii of (a) 2, (b) 4, (c) 5, (d) 6, (e) 10 and (f) 20 mm. The attenuation obtained at the end of the curvature ($\Psi = 180^\circ$) for each radius is 31, 16.3, 12.7, 9.7, 5.1 and 2.7 dB, respectively. The boundaries corresponding to core (dotted line) and cladding (solid line) are also depicted.

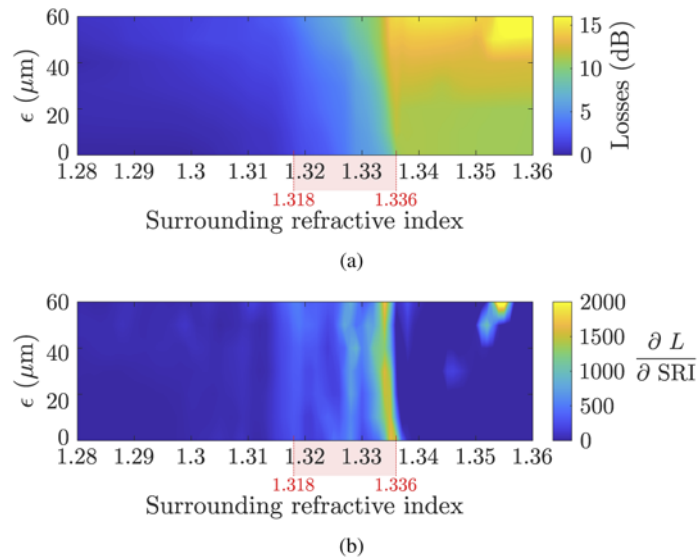


Fig. 5. (a) RSoft simulation of fibre losses (L) due to curvature ($R = 5$ mm) as a function of polishing depth (ϵ) and surrounding refractive index. (b) $\partial L / \partial \text{SRI}$ of the values represented in (a). The SRI range between 1.318 and 1.336 is highlighted, due to its remarkable sensitivity.

For the chosen bending radius value ($R = 5$ mm), the fibre losses L (at $\Psi = 180^\circ$) are simulated for the values given in the corresponding part of Table 2. Specifically, a sweep is performed on the surrounding refractive index (SRI between 1 and 1.36) for different values of polishing depth (ϵ between $0 \mu\text{m}$ and $60 \mu\text{m}$ with steps of $10 \mu\text{m}$). The results are plotted in Fig. 5.

It can be seen that, together with the fibre curvature itself, the polishing of the cladding contributes to increase the sensitivity to the external medium. However, due to its graded-index refractive index profile, the transverse field travels more confined to the axial axis of the fibre. Consequently, there are no evident differences with increasing polishing depth (only a slight increase in losses), even going into the core ($\epsilon \geq 20 \mu\text{m}$). This differs from using a step-index fibre [17]. A polish of about $50 \mu\text{m}$, slightly inside the core, will be a good value to be able to inscribe a sufficient number of periods on the diffraction grating, as detailed in the next section.

4. Diffraction grating operating principle

A diffraction grating will be inscribed on the polished surface. The angles of the diffracted modes (θ_d for transmission, and θ_r for reflection) are related to the wavelength (λ) and grating period (Λ) through the grating equation, both in the transmission (Eq. (7)) and the reflection region (Eq. (8)).

$$n_L \sin \theta_d = n_{core} \sin \theta_i + \frac{\lambda}{\Lambda} p, \quad p \in \mathbb{Z}. \quad (7)$$

$$n_{core} \sin \theta_r = n_{core} \sin \theta_i + \frac{\lambda}{\Lambda} p, \quad p \in \mathbb{Z}. \quad (8)$$

θ_i refers to the angle of the incident wave, p to the diffraction order, n_{core} to the core RI, and n_L to the SRI. These equations only predicts the direction of the modes, not how much power is in them. Figure 6 depicts a schematic of the above.

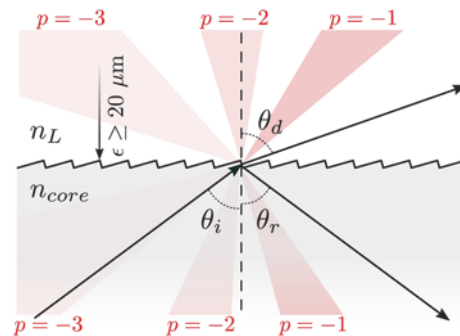


Fig. 6. Diagram of 1-D diffraction grating. The diffraction orders in transmission and reflection are depicted. It is assumed that there is no cladding (removed in polishing).

The grating period chosen must be such as to ensure a low-order grating ($\Lambda > \lambda/n_{core}$) with relevant efficiency in the diffracted orders. For the spectral range to be used ($\lambda \in [1500-1600]$ nm), a grating period $\Lambda = 2 \mu\text{m}$ will be used. According to the selected value $\epsilon = 50 \mu\text{m}$, it is obtained an ellipse with major and minor axes of 1.42 mm and $148 \mu\text{m}$, respectively. This results in the inscription of a grating with more than 700 periods, thus improving the efficiency of the different diffraction orders.

In this case, the appearance of new diffraction orders (as a function of λ and n_L) causes a transfer of energy from the old to the new diffraction orders (Rayleigh anomalies [20,21]). Consequently, there will be transitions or power variations (absorption peaks in short) in the spectrum transmitted and collected in an optical spectrum analyser (OSA). This is the main feature to be exploited in the measurement process.

5. Experimental results and discussion

5.1. *Fs laser setup and inscription parameters*

The inscription of the diffraction grating has been carried out using the optical setup depicted in Fig. 7. A commercial fibre laser chirped pulse amplifier (FLCPA) from CALMAR laser has been applied. It has a 1030 nm wavelength, and 370 fs pulse duration. However, the laser beam is passed through a barium borate crystal (BBO) in order to generate a 515 nm laser beam (Second Harmonic Generation, SHG). After harmonic separation is performed, the previously reduced beam (higher irradiance in the BBO results in higher conversion efficiency) is expanded. The pulse energy (E_p) is controlled by the combination of $\lambda/2$ plate and linear polarizer. Subsequently, a half-wave plate and a quarter wave-plate are arranged in order to have total control of the polarization state of the laser beam. Subsequently, an iris diaphragm is placed to provide a clean wavefront. The laser pulses are tightly focused through a NA = 0.5, $\times 100$ Mitutoyo objective lens. The sample is placed on a nano-resolution XYZ motor stage from Aerotech. Finally, the monitoring and visualization of the inscription process is carried out with a CMOS camera.

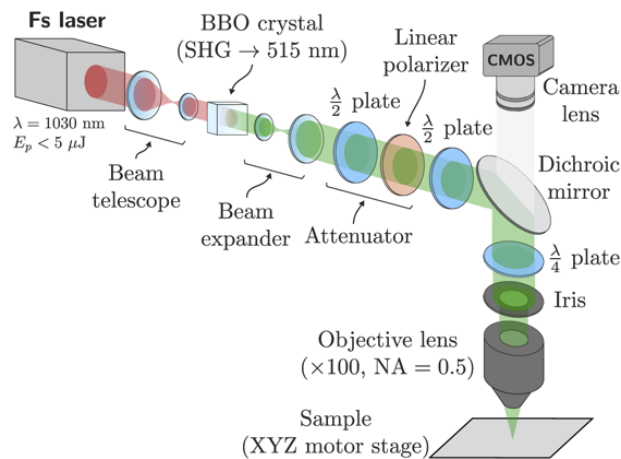


Fig. 7. Femtosecond laser inscription setup.

Once the structure has been polished with ultra-fine vegetable fibre sandpaper, the surface depicted in Fig. 8(a) is obtained. The area corresponding to the cladding corresponds to an ellipse with major and minor axes of 1.41 mm and 148 μm , respectively. According to Eq. (1) and Eq. (2), the ϵ value is 49.2 μm . Fs laser inscription parameters of the diffraction grating are $\Lambda = 2 \mu\text{m}$, grating length of 1.45 mm, grating line length of 160 μm , $E_p = 220 \text{ nJ}$, pulse repetition rate (PRR) of 30 kHz and 1000 pulses/ μm . Figure 8(c) depicts an image of the diffraction grating, with the final complete structure in Fig. 8(d). With the indicated protocol, the repeatability of the sensor is assured.

5.2. *Sensor application*

The applicability of the fabricated structure as a refractometer for aqueous solutions is then verified. For this purpose, transmission measurements are performed using the super-luminescent diode (SLD) light source S5FC1005S (Thorlabs), and the OSA MS9740A (Anritsu), with 30 pm resolution. There is approximately $\sim 1 \text{ m}$ of CYTOP fibre, with single-mode fibre (SMF) connections at both ends.

The liquids used in the measurement process are obtained using different ratios of sucrose-aqueous solution. The RI determination of those liquids has been carried out with the Krüss

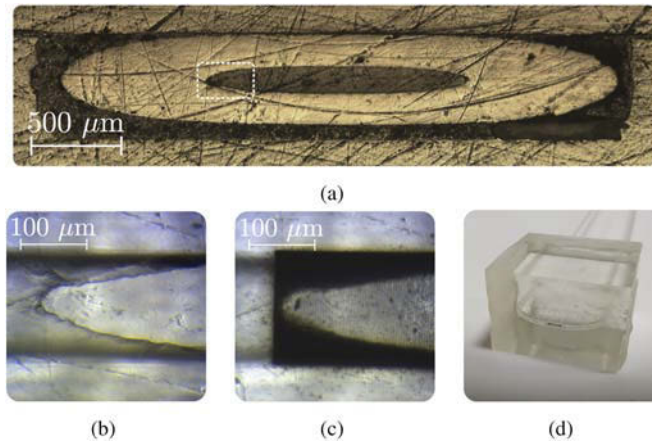


Fig. 8. (a) 5× microscope image of the ellipse generated as a result of polishing, showing both cladding and core, as well as overcladding. 20× microscope images (b) before (c) and after diffraction grating inscription of the region indicated in (a) are also shown. (d) Image of the complete CYTOP-based optical structure.

DR6100 refractometer, at a temperature of $23.9 \pm 0.4^\circ\text{C}$. The RI values, both measured in the yellow doublet D-line of sodium (589.3 nm) and estimated in C-Band (1550 nm), are presented in Table 3. The estimation is made by combining existing literature data [22,23], and Sellmeier coefficients in water [24]. According to the simulation results in Fig. 5, the liquids used are in the RI range of highest sensitivity.

Table 3. Solute concentration, n_D and $n(1550 \text{ nm})$ of the liquids used in the experiments.

Solute concentration ^a	0 g	20 g	40 g	60 g	80 g	100 g
n_D^b	1.3322	1.3353	1.3390	1.3415	1.3438	1.3468
$n(1550 \text{ nm})$	1.3153	1.3184	1.3221	1.3246	1.3269	1.3299

^a $\text{C}_{12}\text{H}_{22}\text{O}_{11}$ grams per 1L H_2O ;

^b $n_D = n(589.3 \text{ nm})$.

Placing the manufactured structure in a fixed position, it is immersed in the different liquids, obtaining the transmission spectra depicted in Fig. 9(a). The measurements are repeated five times, with the uncertainty (95% confidence level, CL) depicted in the shaded region of each curve. Processing the spectra, it is observed that there are six points whose tracking consistently gives a discrimination of n_L with a high sensitivity in the range 1.315–1.33. These are valleys (absorption peaks) 2, 4, 5 and 6 in the figure, and peaks 1 and 3. Figure 9(b) contains the wavelength shift ($\Delta\lambda$) of each of these peaks/valleys for the six liquids used, with the corresponding quadratic fit. In addition to the high coefficient of determination (R^2) of the fits, it is worth noting that there are three obvious trends, i.e. peaks with similar behaviour: 1, 2 and 6 have a higher sensitivity in the range $n_L \in [1.325 - 1.33]$, 4 has its highest sensitivity in the range 1.315–1.32, while 3 and 5, although they have a lower sensitivity, have a higher linearity over the whole range 1.315–1.33 (Table 4).

On the other hand, the fibre losses are also depicted in Fig. 9(c). For $\lambda = 1550 \text{ nm}$, both the experimental results and their quadratic fit, as well as the simulation results (Fig. 5(a)), are shown. Taking into account that the intrinsic losses of the CYTOP fibre have not been taken into account

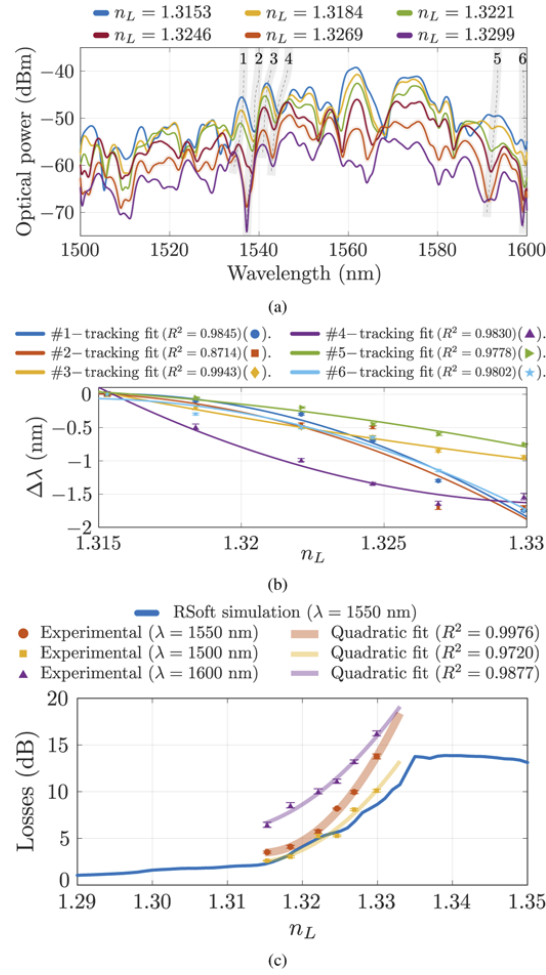


Fig. 9. (a) Transmission spectra when the structure is immersed in liquids with different RI. The 6 peaks and valleys on which the tracking in sensing is performed are highlighted. (b) Wavelength shift ($\Delta\lambda$) of each of the 6 peaks/valleys for the liquids used, with their quadratic fit and error bars (CL = 95%). (c) Simulation and experimental transmission losses for $\lambda = 1550$ nm, as well as experimental results for $\lambda = 1500$ nm and $\lambda = 1600$ nm, with the associated error bars (CL = 95%)

Table 4. Parameters of the quadratic and linear fit of the six curves depicted in Fig. 9(b).

	QUADRATIC FIT: $a_1 n_L^2 + a_2 n_L + a_3$			LINEAR FIT: $b_1 n_L + b_2$ (only b_1 indicated)		
	$a_1 (\frac{\text{nm}^2}{\text{RIU}})$	$a_2 (\frac{\text{nm}}{\text{RIU}})$	$a_3 (\text{nm})$	$n_L \rightarrow 1.315 - 1.32$	$1.32 - 1.325$	$1.325 - 1.33$
#1	-8556	22510	-14802	$-37.56 \frac{\text{nm}}{\text{RIU}}$	$-123.2 \frac{\text{nm}}{\text{RIU}}$	$-208.8 \frac{\text{nm}}{\text{RIU}}$
#2	-7098	18650	-12250	$-54.61 \frac{\text{nm}}{\text{RIU}}$	$-125.6 \frac{\text{nm}}{\text{RIU}}$	$-196.7 \frac{\text{nm}}{\text{RIU}}$
#3	1020	-2765	1873	$-78.21 \frac{\text{nm}}{\text{RIU}}$	$-68 \frac{\text{nm}}{\text{RIU}}$	$-57.8 \frac{\text{nm}}{\text{RIU}}$
#4	6420	-17100	11380	$-179.7 \frac{\text{nm}}{\text{RIU}}$	$-115.5 \frac{\text{nm}}{\text{RIU}}$	$-51.25 \frac{\text{nm}}{\text{RIU}}$
#5	-1827	4776	-3122	$-36.93 \frac{\text{nm}}{\text{RIU}}$	$-55.21 \frac{\text{nm}}{\text{RIU}}$	$-73.49 \frac{\text{nm}}{\text{RIU}}$
#6	-6879	18080	-11890	$-42.53 \frac{\text{nm}}{\text{RIU}}$	$-111.4 \frac{\text{nm}}{\text{RIU}}$	$-180.2 \frac{\text{nm}}{\text{RIU}}$

in the simulation, the similarity is remarkable. In fact, the Pearson correlation coefficient between the simulation curve for $n_L \in [1.315 - 1.333]$ and the quadratic fit of the experimental results is $\rho = 0.9799$. In this range, the sensitivities are 695.9 dB/RIU (experimental measurements) and 422.5 dB/RIU (simulation). Finally, the experimentally obtained losses for the 1500 and 1600 nm wavelengths are also depicted in order to observe the trend. Considering that sensitivities above 120 nm/RIU are obtained in any of the three defined ranges (Table 4), it is possible to sense changes in SRI when they are in the order of 10^{-3} ($\Delta\lambda \geq 0.12$ nm) or even $2.5 \cdot 10^{-4}$ ($\Delta\lambda \geq 30$ pm). Only peak #4 presents an uncertainty higher than the OSA resolution (30 pm), especially in the first of the linear sections defined in Table 4. In that range ($n_L \in [1.315 - 1.32]$), the detection occurs for $\Delta\lambda \geq 57$ pm, but the sensitivity in that section is -179.7 nm/RIU, so it is possible to detect changes in SRI of up to $\sim 3.1 \cdot 10^{-4}$. Peaks with a positive concavity, such as #4, are used as sensing points for the lower range of the sensing zone, due to their high sensitivity.

5.3. Temperature cross-sensitivity

Temperature cross-sensitivity has an important influence in terms of refractive index measurement.

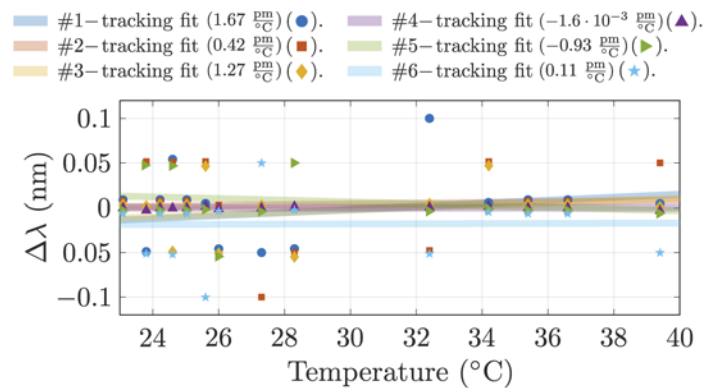


Fig. 10. Wavelength shift ($\Delta\lambda$) of each peak/valley as a function of temperature. The structure has been immersed in water ($n_L = 1.3153$), and a temperature sweep between 23 and 40 °C has been performed. A linear fit is made, with the slope of each fit. It should be noted that the wavelength step in the spectrum is 50 pm.

The characteristics of the diffraction grating are modified with temperature, as is the period (Λ). Firstly, it is important to note that the coefficient of linear thermal expansion (CLTE) of CYTOP is $\sim 7.4 \cdot 10^{-5} \text{ }^\circ\text{C}^{-1}$, which is slightly lower than PMMA. Therefore, it is not a relevant factor here, even less so in a temperature range below 30 °C. To evaluate the behaviour of the SRI sensor, a temperature sweep between 23 °C (room temperature) and 40 °C is performed. In the measurement process, the device is immersed in water ($n_L = 1.3153$), and the peaks/valleys indicated in Fig. 9(a) are tracked. The variation of the refractive index of the liquid in this temperature range is less than $5 \cdot 10^{-4}$. The results obtained are depicted in Fig. 10. The most pronounced variation is observed at peak #1, with 1.67 pm/°C. In any case, this is a value that can be considered negligible, since it gives rise to an error in the SRI measurement that is in the order of 10^{-5} . It can therefore be concluded that the measurement of the surrounding refractive index is insensitive to the temperature of the fluid.

6. Discussion

To conclude the paper, it is interesting to briefly outline the main innovations and advantages compared to existing work on fibre-based refractometers. In a 2019 review, Urrutia *et al.* present the state of the art associated with optical fibre refractometers [25], classifying them according to

whether they are interferometers, grating-based structures, or resonance-based structures (coating). Although it can be concluded that there is not a great difference in performance between these three groups, it can be highlighted that tilted fibre Bragg gratings (TFBG) have been traditionally used as they are absolute refractometers in a wide wavelength range [26,27]. Moreover, they are relatively robust and simple, as they do not need specialty fibres, nor modifications of their geometry that degrade their practical use from a commercial point of view. With an accuracy of $\pm 5 \cdot 10^{-5}$, the grating-based refractometer presented in [26] indicates that works are beginning to exist that obtain comparable performances to the Abbe refractometer.

TFBG-based refractometers have even been developed on polymer fibres [28]. These are custom PMMA fibers with a core diameter of 8.2 μm and $\text{NA} = 0.23$, which gives rise to a few-mode behaviour (4 guided modes). Although the performance is lower than silica single-mode fibres, sensitivities of up to $\sim 13 \text{ nm/RIU}$ are achieved. They also allow to increase their high sensitivity measurement range up to $\text{SRI} = 1.49$, compared to silica fibers, with a range of up to about $\text{SRI} = 1.45$. However, commercially available perfluorinated fibres have a highly multimode behaviour, which makes it impossible to use TFBGs to detect SRI with high accuracy. The great advantage of using polishing in combination with diffraction gratings is that, by eliminating cladding in a curved area, it is possible to induce most of the guided modes to interact with the external medium and condition their propagation as a function of SRI. Also, although these fibres do not allow a high sensitivity region as wide as PMMA fibres, they do have a maximum sensitivity region of around $\text{SRI} = 1.34$. This makes them very suitable for applications that require a high sensitivity region. This makes them very suitable for applications requiring discrimination of aqueous solutions.

7. Conclusion

To the authors' knowledge, this is the first work using perfluorinated polymer fibres for the sensing of the surrounding refractive index. It also presents the novelty of using an in-fibre diffraction grating for the detection. This optical structure, inscribed with a femtosecond laser on a previously polished curvature zone, makes it possible to modify the diffraction orders transmitted (losses) and reflected (propagated by the fibre) as a function of the SRI, thus obtaining a specific "fingerprint" of the external liquid. Due to the RI of the fibre used, this is a device designed for use in aqueous solutions, with a potential use in biomedical applications. Also, as can be deduced from its final presentation, depicted in several images of the work, it is easily encapsulated for a robust practical use. It has a maximum sensitivity of -208.8 nm/RIU , can detect changes in SRI of around $2.5 \cdot 10^{-4}$, and is insensitive to temperature, thus avoiding cross-sensitivity issues.

Funding. Ministerio de Ciencia, Innovación y Universidades, Agencia Estatal de Investigación and FEDER funds of European Commission (PID2019-107270RB-C21 by MCIN/AEI/10.13039/501100011033); Ministerio de Educación, Cultura y Deporte of Spain (PhD grant FPU2018/02797).

Disclosures. The authors declare no conflicts of interest.

Data availability. Data underlying the results presented in this paper are not publicly available at this time but may be obtained from the authors upon reasonable request.

References

1. D. Pallarés-Aldeiturriaga, P. Roldán-Varona, L. Rodríguez-Cobo, and J. M. López-Higuera, "Optical fiber sensors by direct laser processing: A review," *Sensors* **20**(23), 6971 (2020).
2. K. Peters, "Polymer optical fiber sensors—a review," *Smart Mater. Struct.* **20**(1), 013002 (2011).
3. L. Bilro, N. Alberto, J. L. Pinto, and R. Nogueira, "Optical sensors based on plastic fibers," *Sensors* **12**(9), 12184–12207 (2012).
4. J. Zubia and J. Arrue, "Plastic optical fibers: An introduction to their technological processes and applications," *Opt. Fiber Technol.* **7**(2), 101–140 (2001).

5. N. Yoshihara, "Low-loss, high-bandwidth fluorinated POF for visible to 1.3- μm wavelengths," in *OFC '98. Optical Fiber Communication Conference and Exhibit. Technical Digest. Conference Edition. 1998 OSA Technical Digest Series Vol.2 (IEEE Cat. No.98CH36177)*, (Opt. Soc. America, 1998).
6. M. Naritomi, "CYTOP amorphous perfluoropolymer for low loss POF," *POF Asia Pacific Forum '96* (1996).
7. A. Lacraz, M. Polis, A. Theodosiou, C. Koutsides, and K. Kalli, "Femtosecond laser inscribed Bragg gratings in low loss CYTOP polymer optical fiber," *IEEE Photonics Technol. Lett.* **27**(7), 693–696 (2015).
8. A. Theodosiou and K. Kalli, "Recent trends and advances of fibre Bragg grating sensors in CYTOP polymer optical fibres," *Opt. Fiber Technol.* **54**, 102079 (2020).
9. Y.-G. Nan, D. Kinet, K. Chah, I. Chapalo, C. Caucheteur, and P. Mégret, "Ultra-fast fiber Bragg grating inscription in CYTOP polymer optical fibers using phase mask and 400 nm femtosecond laser," *Opt. Express* **29**(16), 25824–25835 (2021).
10. C. Broadway, D. Kinet, A. Theodosiou, K. Kalli, A. Gusarov, C. Caucheteur, and P. Mégret, "CYTOP fibre Bragg grating sensors for harsh radiation environments," *Sensors* **19**(13), 2853 (2019).
11. A. G. Leal-Junior, A. Theodosiou, C. A. R. Diaz, L. M. Avellar, K. Kalli, C. Marques, and A. Frizera, "FPI-POFBG angular movement sensor inscribed in CYTOP fibers with dynamic angle compensator," *IEEE Sens. J.* **20**(11), 5962–5969 (2020).
12. A. G. Leal-Junior, H. R. O. Rocha, A. Theodosiou, A. Frizera, C. Marques, K. Kalli, and M. R. N. Ribeiro, "Optimizing linearity and sensitivity of 3D-printed diaphragms with chirped FBGs in CYTOP fibers," *IEEE Access* **8**, 31983–31991 (2020).
13. A. G. Leal-Junior, A. Theodosiou, R. Min, J. Casas, C. R. Diaz, W. M. D. Santos, M. J. Pontes, A. A. G. Siqueira, C. Marques, K. Kalli, and A. Frizera, "Quasi-distributed torque and displacement sensing on a series elastic actuator's spring using FBG arrays inscribed in CYTOP fibers," *IEEE Sens. J.* **19**(11), 4054–4061 (2019).
14. A. Theodosiou, X. Hu, C. Caucheteur, and K. Kalli, "Bragg gratings and Fabry-Perot cavities in low-loss multimode CYTOP polymer fiber," *IEEE Photonics Technol. Lett.* **30**(9), 857–860 (2018).
15. A. Theodosiou, A. Lacraz, A. Stassis, C. Koutsides, M. Komodromos, and K. Kalli, "Plane-by-plane femtosecond laser inscription method for single-peak Bragg gratings in multimode CYTOP polymer optical fiber," *J. Lightwave Technol.* **35**(24), 5404–5410 (2017).
16. M. Ochoa, J. F. Algorri, P. Roldán-Varona, L. Rodríguez-Cobo, and J. M. López-Higuera, "Recent advances in biomedical photonic sensors: A focus on optical-fibre-based sensing," *Sensors* **21**(19), 6469 (2021).
17. M. Lomer, A. Quintela, M. López-Amo, J. Zubia, and J. López-Higuera, "A quasi-distributed level sensor based on a bent side-polished plastic optical fibre cable," *Meas. Sci. Technol.* **18**(7), 2261–2267 (2007).
18. C. Schulze, A. Lorenz, D. Flamm, A. Hartung, S. Schröter, H. Bartelt, and M. Duparré, "Mode resolved bend loss in few-mode optical fibers," *Opt. Express* **21**(3), 3170–3181 (2013).
19. D. Pallares-Aldeiturriaga, L. Rodríguez-Cobo, A. Quintela, and J. M. Lopez-Higuera, "Curvature sensor based on In-Fiber Mach-Zehnder interferometer inscribed with femtosecond laser," *J. Lightwave Technol.* **35**(21), 4624–4628 (2017).
20. J. E. Harvey and R. N. Pfisterer, "Understanding diffraction grating behavior: including conical diffraction and Rayleigh anomalies from transmission gratings," *Opt. Eng.* **58**(08), 1 (2019).
21. M. S. Amin, J. W. Yoon, and R. Magnusson, "Optical transmission filters with coexisting guided-mode resonance and Rayleigh anomaly," *Appl. Phys. Lett.* **103**(13), 131106 (2013).
22. J. E. Saunders, C. Sanders, H. Chen, and H.-P. Loock, "Refractive indices of common solvents and solutions at 1550 nm," *Appl. Opt.* **55**(4), 947–953 (2016).
23. G. M. Hale and M. R. Querry, "Optical constants of water in the 200-nm to 200- μm wavelength region," *Appl. Opt.* **12**(3), 555–563 (1973).
24. M. F. H. Arif and M. J. H. Biddut, "Enhancement of relative sensitivity of photonic crystal fiber with high birefringence and low confinement loss," *Optik* **131**, 697–704 (2017).
25. A. Urrutia, I. D. Villar, P. Zubieta, and C. R. Zamarreño, "A comprehensive review of optical fiber refractometers: Toward a standard comparative criterion," *Laser Photonics Rev.* **13**(11), 1900094 (2019).
26. W. Zhou, Y. Zhou, and J. Albert, "A true fiber optic refractometer," *Laser Photonics Rev.* **11**(1), 1600157 (2017).
27. Z. Liu, C. Shen, Y. Xiao, J. Gong, J. Wang, T. Lang, C. Zhao, C. Huang, Y. Jin, X. Dong, Y. Zhang, Z. Jing, W. Peng, and Y. Semenova, "Liquid surface tension and refractive index sensor based on a tilted fiber Bragg grating," *J. Opt. Soc. Am. B* **35**(6), 1282–1287 (2018).
28. X. Hu, C.-F. J. Pun, H.-Y. Tam, P. Mégret, and C. Caucheteur, "Tilted bragg gratings in step-index polymer optical fiber," *Opt. Lett.* **39**(24), 6835–6838 (2014).